applied sciences

MDPI

Article

Application of Spread-Spectrum Induced Polarization (SSIP) Technology in W-Sn Mineral Exploration (Xitian Mining District, SE China)

Xiaoqiang Li [1], Haifei Liu [1,2,*], Yingjie Zhao [1], Yuhao Zhang [1] and Daowei Zhu [1]

[1] School of Geosciences and Info-Physics, Central South University, Changsha 410083, China; 235011102@csu.edu.cn (X.L.); zhao_yj404@163.com (Y.Z.); 19918519339@163.com (Y.Z.); zhudaowei66@163.com (D.Z.)

[2] Hunan Key Laboratory of Nonferrous Resources and Geological Hazard Detection, Central South University, Changsha 410083, China

* Correspondence: liuhaifei@126.com; Tel.: +86-138-7337-8983

Abstract: As strategic critical metals, tungsten (W) and tin (Sn) require efficient exploration methods for effective resource development. This study implemented an advanced spread-spectrum induced polarization (SSIP) method in the Xitian mining district of southern China. Through optimized survey system configuration (maximum current electrode spacing of 5200 m, 12-channel acquisition, and five discrete frequency points), we achieved significant advancements: (1) a penetration depth of 1200 m, and (2) three- to five-times higher data acquisition efficiency compared to conventional symmetrical quadrupole arrays. Inversion results of resistivity and chargeability profiles from two parallel survey lines (total length 2.4 km) demonstrated an 85% spatial correlation between resistivity and chargeability anomalies, successfully identifying three mineralized veins. Drill-hole verification confirmed the presence of greisen veins (characterized by low resistivity <100 $\Omega \cdot$ m and high chargeability > 3%) and skarn veins (moderate resistivity 150–200 $\Omega \cdot$ m and chargeability 1.5–2%). The method exhibits a detection sensitivity of 0.5% chargeability contrast for deep-seated W-Sn polymetallic deposits, providing quantitative technical references for similar deposit exploration.

Keywords: W-Sn orebody; Xitian mining district; spread-spectrum induced polarization (SSIP); resistivity and chargeability profiles

check for updates

Academic Editors: Nikolaos Koukouzas and Haiqing Yang

Received: 15 April 2025
Revised: 27 May 2025
Accepted: 5 June 2025
Published: 9 June 2025

Citation: Li, X.; Liu, H.; Zhao, Y.; Zhang, Y.; Zhu, D. Application of Spread-Spectrum Induced Polarization (SSIP) Technology in W-Sn Mineral Exploration (Xitian Mining District, SE China). *Appl. Sci.* **2025**, *15*, 6480. https://doi.org/10.3390/app15126480

Copyright: © 2025 by the authors. Licensee MDPI, Basel, Switzerland. This article is an open access article distributed under the terms and conditions of the Creative Commons Attribution (CC BY) license (https://creativecommons.org/licenses/by/4.0/).

1. Introduction

Tungsten (W) and tin (Sn) are important metals. Accompanied by the greater demand for W-Sn, the study and exploitation of W-Sn deposits have long been a hot topic [1–13]. China ranks first in the world in terms of tungsten resources and reserves and has some of the largest tungsten deposits [14]. The Nanling region in the central part of South China accounts for more than 92% of Chinese tungsten resources; thus, it is the most important tungsten–tin (W–Sn) polymetallic province, and it has a close spatial relationship with the Yanshanian granites [15–18]. The Xitian W–Sn polymetallic district is one of the most significant finds of tungsten–tin mineral resources in the Nanling area (W–Sn reserves $\geq 30 \times 10^4$ t) [19]. It is an area with great potential for W and Sn resources [20–22].

Mineral exploration is an indispensable component in the development of metallic mineral resources such as W and Sn, where geophysical methods play a pivotal role [23–32]. The direct current (DC) resistivity method, as a widely utilized geophysical technique,

has been extensively employed in mineral exploration [33–35]. It demonstrates distinct advantages, including precise target delineation, high operational efficiency, and strong anti-interference capabilities [36]. As a specialized variant of the DC resistivity method, induced polarization (IP) demonstrates exceptional value and efficacy in metallogenic studies and mineral exploration [37–46]. The spectral induced polarization (SSIP) technique, as an emerging exploration method in induced polarization surveys, has demonstrated outstanding performance in mineral exploration [47,48].

1.1. Regional Geological Background

As shown in Figure 1, the South China block (SCB) was formed by the amalgamation of the Yangtze block (YZB) in the northwest and the Cathaysia block (CAB) in the southeast. The Nanling region is situated in the central part of the SCB, with the Xitian ore field located in the central Nanling area—specifically at the western outer contact zone of the dumbbell-shaped Xitian granite pluton's handle section, within the Longshang ore block.

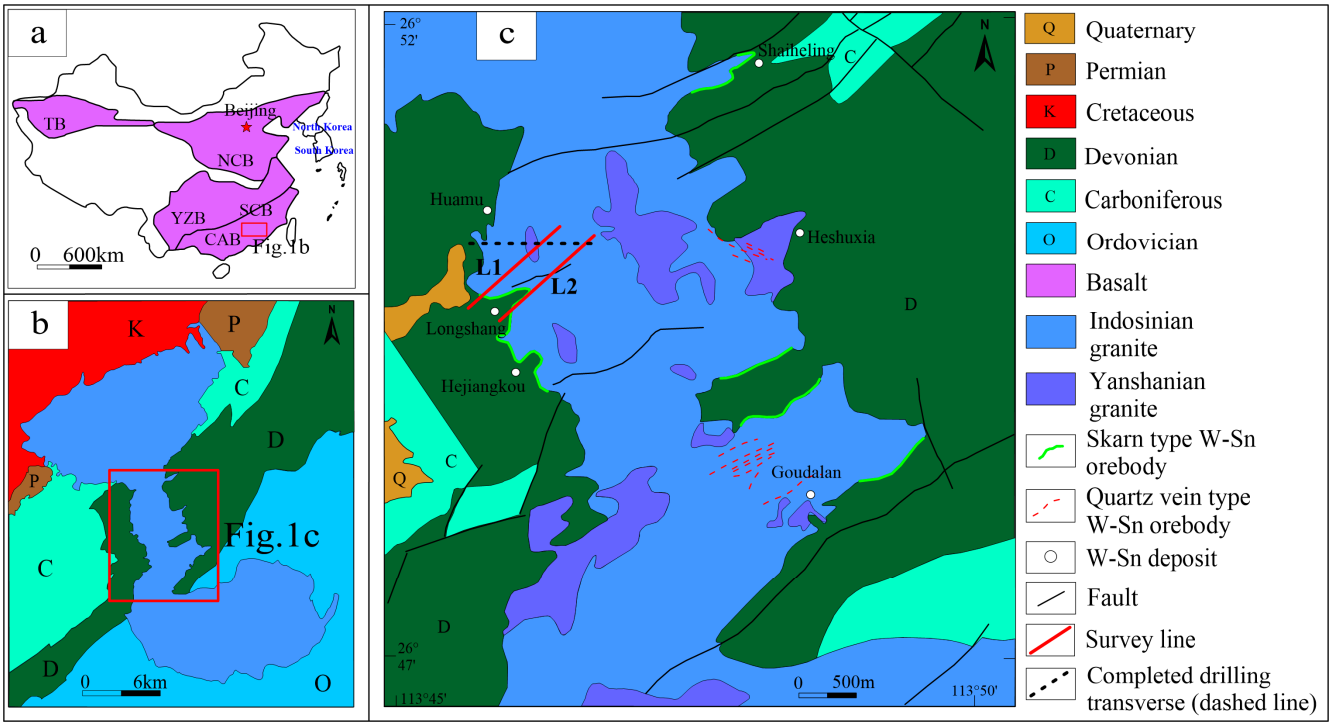

Figure 1. Comprehensive geological map of the Xitian mining district: (**a**) geological sketch map of China with different geological blocks and neighboring countries (modified from [49]), (**b**) schematic geological map of the Xitian W–Sn ore deposits (modified from [50]), and (**c**) detailed schematic geological map of the Xitian W-Sn ore deposit field (modified from [49]). TB: Tarim block, CAB: Cathaysian block, NCB: North China block, SCB: South China block, YZB: Yangtze block.

The study area primarily develops the Upper Devonian Xikuangshan Formation, the Shetianqiao Formation, and the Middle Devonian Qiziqiao Formation. The Xikuangshan Formation can be divided into upper and lower members: the upper member consists of grayish-white, medium-thick-bedded mica-bearing quartz sandstone intercalated with mudstone, approximately 100 m thick; the lower member comprises gray to bluish-gray banded limestone with sandy-argillaceous bands and medium-thick bedding, about 70 m thick, conformably overlying the Shetianqiao Formation. The Shetianqiao Formation has a total thickness of 200 m to 250 m, with its upper part being gray to gray-yellow, medium-thick-bedded mica-bearing quartz sandstone intercalated with sandy mudstone; the middle part consists of gray-white to gray-yellow, medium-fine-grained quartz sandstone with individual beds 40 cm to 80 cm thick and quartz content exceeding 90%, weathering to

a sugary texture; the lower part is gray to gray-white, medium-thick-bedded siltstone intercalated with mudstone, conformably overlying the Qiziqiao Formation. The Qiziqiao Formation is over 200 m thick, with its upper part being gray to gray-white limestone intercalated with calcareous dolomite and marl, weathering yellowish-brown and partially marmorized; the middle part shows interbedded dolomite and limestone with banded limestone and widely developed marbleization; the lower part consists of gray-white to gray thin to medium-thick bedded calcareous dolomite intercalated with mudstone, commonly containing diopside alteration, serving as the main host horizon for tungsten–tin skarn mineralization in the area, conformably overlying the Tiaomajian Formation.

The mining area generally exhibits an approximate homoclinal structure, with strata striking ≈ 325 °NW and dipping 50 °SW to 70 °SW. The fault system develops a NE-trending fault (F1) that crosses a ravine about 20 m west of the main shaft. Another fault (F2) strikes ≈ 335 °NW and dipping 50 °NE to 70 °NE. The fracture zone is 5 m to 20 m wide, showing silicification and greisenization within the zone, where the orebodies in the working area are hosted.

Approximately 1700 m northeast of the mine, the Xitian pluton is exposed, which was formed during the Yanshanian period and consists of medium-fine- to medium-grained porphyritic biotite granite. The wall-rock alterations in the working area mainly include silicification, skarnization, greisenization, pyritization, and marbleization. The structural complexity of the mining area is classified as simple type. Influenced by the Indosinian–Yanshanian tectonic movements, the wall rocks exhibit well-developed joints and fractures, providing favorable ore-hosting spaces for vein-type W-Sn mineralization.

1.2. Electrical Properties of Rocks and Ores

The resistivity and chargeability parameters of typical rocks and ores in the mining area are detailed in Table 1, which reveals significant correlations between different lithologies and SSIP anomalies. High-resistivity rocks, such as granite, marble, and quartz sandstone (resistivity > 350 $\Omega \cdot$ m), generally exhibit low chargeability (<1%), primarily due to the insulating properties of their silicate mineral composition, which restricts charge migration. In contrast, mineralized bodies display distinct low-resistivity and high-chargeability characteristics: vein-type orebodies are most prominent with extremely low resistivity (55 $\Omega \cdot$ m) and exceptionally high chargeability (41%), resulting from continuous electronic conduction networks formed by sulfide minerals coupled with strong polarization at metal–electrolyte interfaces. Although disseminated tungsten–tin ores show relatively higher resistivity (206 $\Omega \cdot$ m), their 2.1% chargeability remains significantly elevated compared to wall rocks, reflecting the electrode polarization effects of isolated metal particles. Particularly noteworthy are pyrite and carbonaceous shale, which, despite their moderate resistivity (200–290 $\Omega \cdot$ m), generate high chargeability anomalies of 11% and 3.7% respectively—the former originating from electrochemical noise caused by surface redox reactions, and the latter associated with semiconducting properties induced by graphitized organic matter. These interference sources substantially increase the complexity of SSIP data interpretation. The variations in electrical parameters of skarn (360 $\Omega \cdot$ m/0.35%) and scheelite-bearing marble (90 $\Omega \cdot$ m/0.25%) directly reflect differing degrees of metallic mineral introduction during hydrothermal alteration. These electrical property differences provide crucial criteria for distinguishing mineralization-related anomalies from interference anomalies in SSIP exploration. Of particular significance, granite samples collected from the pluton top and near contact zones with sedimentary rocks exhibit markedly reduced resistivity values compared to regional background levels.

Table 1. Statistical table of electrical parameters of rock ore in the mining area.

Specimen Type	Average Resistivity (Ω·m)	Average Chargeability (%)
Medium-fine- to medium-grained porphyritic biotite granite	430	0.5
Quartz sandstone	380	0.6
Marble	520	0.3
Skarn	360	0.35
Carbonaceous shale	290	3.7
Siltstone	620	0.05
Mica-bearing quartz sandstone	170	0.8
Pyrite	200	11
Scheelite-bearing marble	90	0.25
Disseminated tungsten–tin ore	206	2.1
Disseminated sulfide-bearing tin–tungsten (molybdenum) ore	126	13
Vein-type orebody	55	41

2. Materials and Methods

This study investigates the Xitian mining district in southeastern China, a region with abundant tungsten–tin resources, where conventional electrical methods exhibit significant limitations in deep orebody exploration. To overcome the challenges of inadequate detection depth, interpretational ambiguity, and low spatial resolution for skarn- and greisen-type mineralization, we innovatively applied SSIP with a 5200 m large-electrode-spacing configuration and 12-channel synchronous acquisition system, achieving an unprecedented exploration depth of 1200 m. The 0.0625 Hz to 1 Hz spread-spectrum IP measurements enabled effective discrimination between mineralized bodies and carbonaceous interference through integrated chargeability–resistivity analysis.

The acquired data were processed, interpreted, and discussed, leading to the delineation of skarn-type and greisen-type mineralization based on the regional geological setting. The distribution of quartz sandstone, sandy mudstone, limestone, and marble was mapped, as well as the undulating morphology of dikes and granite. Drill-hole data verified these interpretations, confirming the effectiveness of the SSIP method for mineral exploration.

2.1. Data Acquisition

Data acquisition was conducted using the GS2IP broadband IP system developed by Central South University. This equipment features simultaneous transmission/reception of pseudo-random spread-spectrum signals, multi-channel array synchronous observation (expandable up to 1200 channels), and real-time calculation/display of amplitude and relative phase parameters at multiple frequencies. The survey deployed two profiles with measurement arrays shorter than the total profile length (as shown in Figure 1). Each profile measured 5200 m (with a 1200 m measurement array length) at 40 m station intervals. When selecting the transmission frequency band, a narrow frequency range reduces both depth and mineral resolution, while a wider range improves resolution but increases noise interference and inversion complexity. To balance deep detection capability with the polarization response of target minerals and minimize electromagnetic coupling, transmission frequencies were set at 0.0625 Hz, 0.125 Hz, 0.25 Hz, 0.5 Hz, and 1 Hz. Each measurement array covered 440 m (12 channels), requiring three array movements per profile. The current injection and measurement point distributions are detailed in Table 2, where data entries indicate positions along the profile—e.g., current electrodes

"(A,B)" at "(180,260)" denote electrode A positioned at 180 m and electrode B at 260 m from the profile origin. For fixed current electrode positions (e.g., "(A,B)" at "(180,260)"), measurement electrodes "(P,Pn)" sequentially occupied positions "(0,40), (40,80), (80,120), (120,160), (160,200), (200,240), (240,280), (280,320), (320,360), (360,400), and (400,440)". The current electrodes then advanced to the next position "(140,300)" while repeating the measurement electrode sequence. This process (illustrated in Figure 2) continued until the entire profile was completed through successive array deployments. The electrode spacing can be appropriately selected based on the size and burial depth of the target body.

Table 2. Distribution of power supply and measurement points.

Current Electrode (A,B) (m)	Potential Electrode (P,Pn) (m)
(180,260);(140,300);(100,340);(60,380);(20,420);(−40,480); (−80,520);(−130,570);(−190,630);(−260,700);(−340,780); (−440,880);(−590,1030);(−790,1230);(−1040,1480); (−1340,1780);(−1640,2080);(−2040,2480)	(0,40);(40,80);(80,120);(120,160); (160,200);(200,240);(240,280); (280,320);(320,360);(360,400);(400,440)
(580,660);(540,700);(500,740);(460,780);(420,820);(360,880); (320,920);(270,970);(210,1030);(140,1100);(60,1180); (−40,1280);(−190,1430);(−640,1880);(−940,2180); (−1240,2480);(−1640,2880)	(400,440);(440,480);(480,520);(520,560); (560,600);(600,640);(640,680);(680,720); (720,760);(760,800);(800,840)
(940,1020);(900,1060);(860,1100);(780,1180);(720,1240); (680,1280);(630,1330);(570,1390);(500,1460);(420,1540); (320,1640);(280,2240);(170,1790);(−30,1990);(−580,2540); (−880,2840);(−1280,3240)	(760,800);(800,840);(840,880);(880,920); (920,960);(960,1000);(1000,1040); (1040,1080);(1080,1120);(1120,1160); (1160,1200)

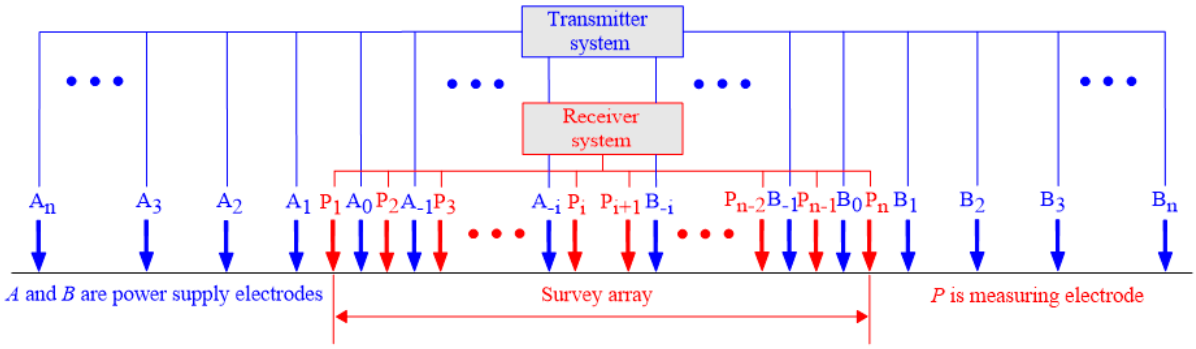

Figure 2. Schematic diagram of the arrangement of multi-channel observations at large pole distances.

The survey area is located in the mountainous region of southern Hunan, where environmental interference during data acquisition was minimal. Standardized operational procedures were implemented throughout the data collection process, complemented by the designed large-spacing multi-channel observation array. Consequently, the acquired data exhibit excellent quality and high reliability.

2.2. SSIP Technology

The SSIP method is a frequency-domain IP technique that transmits pseudo-random m-sequence signals and measures the potential response to obtain resistivity, relative phase, and frequency dispersion parameters [51]. By emitting spread-spectrum signals and receiving potential measurements, this spectral IP method acquires multiple observation parameters with large data volumes and strong anti-interference capabilities; it enables effective detection of metallic sulfide deposits, discrimination of graphite interference, identification of alteration zones, and enhanced targeting accuracy for deep-seated concealed ores through complex resistivity spectral analysis in combination with other geophysical

methods, demonstrating excellent application results in mineral exploration [52]. It shows promising potential for mid-deep mineral exploration.

The SSIP method can effectively identify the co-occurrence characteristics of tungsten (W) and tin (Sn) minerals by analyzing the frequency-dependent responses of complex resistivity and the phase angle. Due to its semiconducting properties, wolframite ((Fe,Mn)WO_4) exhibits significant polarization in the low-frequency range (0.1 Hz to 10 Hz), with phase angle peaks typically below 1 Hz and longer relaxation times (1 s to 10 s). In contrast, cassiterite (SnO_2), influenced by surface redox reactions, primarily responds in the mid-frequency range (1 Hz to 100 Hz), displaying shorter relaxation times (0.01 s to 0.1 s). When these minerals coexist, SSIP spectra demonstrate superposition effects: higher tungsten content enhances low-frequency phase angles and shifts the spectrum toward lower frequencies, whereas higher tin content strengthens mid-frequency responses and accelerates high-frequency attenuation. If their proportions are similar, a bimodal or broad-peak feature may emerge. Additionally, high-frequency signals (>100 Hz) are susceptible to interference from other conductive minerals or electrolytes, necessitating Cole–Cole model inversion for accurate mineralogical discrimination.

The apparent resistivity at different frequencies ($\rho_s(f)$) can be calculated as follows, based on the observed potential differences and supplied currents at corresponding frequencies:

$$\rho_s(f) = K\frac{\Delta V(f)}{I} \tag{1}$$

To obtain a significant induced polarization effect, the apparent chargeability F_s is calculated by selecting a lower-frequency potential difference $\Delta V(f_L)$ and a higher-frequency potential difference $\Delta V(f_H)$ from the multi-frequency potential differences, as follows:

$$F_s = \frac{\Delta V(f_L) - \Delta V(f_H)}{\Delta V(f_L)} \times 100\% \tag{2}$$

2.3. Observation Array Design

To increase exploration depth and improve field data acquisition efficiency, we designed a large-spacing multi-channel observation array, as shown in Figure 2.

During field operations, the measurement electrode array $P_1, P_2, \ldots, P_{n-1}, P_n$ of the multi-channel receiving system is first deployed along the survey line. The current electrode pair AB is progressively expanded outward from the center of the measurement array, with all adjacent electrode pairs simultaneously receiving signals during each current injection. As the AB pair moves from the inner to outer sections of the array, the electrode spacing increases arithmetically within the measurement array to acquire shallow geoelectric information, while outside the measurement array, the current electrode spacing increases by multiples of the measurement electrode interval. For longer survey profiles, multiple measurement arrays need to be deployed sequentially to complete the survey.

During the first measurement array deployment, the current electrode spacing AB is gradually increased from minimum to maximum (up to A_nB_n), completing the first array survey. Subsequently, the entire measurement array is advanced forward by one array length, and the current electrode spacing AB is progressively decreased from maximum to minimum (down to $A_{-i}B_{-i}$) to complete the second array survey. This alternating process continues until the entire profile is surveyed. The actual key configuration parameters of the exploration array are shown in Table 3.

By systematically increasing the current electrode spacing, measurement results reflecting the electrical property variations from shallow to deep subsurface media are obtained. The resistivity amplitude spectrum and chargeability are then inverted to yield 2D inver-

sion sections depicting the subsurface distribution of electrical properties and induced polarization characteristics.

Table 3. Key configuration parameters of the SSIP survey array.

Parameter	Value
Measurement Array Length	1200 m
Current Electrode Span	5200 m
Minimum Electrode Spacing (Current)	80 m
Minimum Electrode Spacing (Potential)	40 m
Array Shift Distance	400 m
Ground Resistance	<2000 Ω
Power Supply Current	<10 A
Transmission Frequency	0.0625 Hz to 1 Hz

2.4. SSIP Equivalent Inversion Method

Forward modeling serves as the foundation for inversion in geophysics, where finite element method (FEM) simulations are conducted prior to inversion. Originally developed in elasticity mechanics, FEM is particularly suitable for geophysical problems involving complex property distributions. Its standardized solution process and other advantages have led to widespread application in geophysical studies.

In the limiting cases of low frequency $f_L \to 0$ and high frequency $f_H \to \infty$, it can be concluded that the limiting chargeability equals the limiting polarizability. Since chargeability reflects the intensity of induced polarization effects and is equivalent to polarizability and metal factor in anomaly detection, this study treats spread-spectrum IP data as DC IP data for inversion. Based on Seigel's induced polarization theory, the geoelectric model is jointly described using resistivity and polarizability parameters, with polarizability defined within the range [0,1) and assumed to vary significantly less than resistivity. For the inversion of resistivity and polarizability data, resistivity inversion is typically completed first, followed by polarizability inversion with the resistivity model fixed.

First, the objective function for resistivity inversion is constructed under the least squares criterion as follows:

$$\Phi_\rho(\boldsymbol{m}_\rho) = \left\| \boldsymbol{W}_\rho \left[\boldsymbol{d}_{\rho a} - \boldsymbol{d}_{\rho c}(\boldsymbol{m}_\rho) \right] \right\|_2^{\,2} + \lambda_{\rho s} \left\| \boldsymbol{S}\boldsymbol{m}_\rho \right\|_2^{\,2} + \lambda_{\rho b} \left\| \boldsymbol{B}\left[\boldsymbol{m}_\rho - \boldsymbol{m}_{\rho b} \right] \right\|_2^{\,2} \tag{3}$$

where the first term on the right side is the data misfit term and $\boldsymbol{W}_\rho$ is the data weighting matrix used to suppress interference noise in the data. $\boldsymbol{d}_{\rho a} = ln(\rho_a)$, where ρ_a is the measured apparent resistivity, and $\boldsymbol{d}_{\rho c}(m_\rho) = ln(\rho_c)$, where ρ_c is the modeled apparent resistivity. The model parameters satisfy $\boldsymbol{m}_\rho = ln(\rho)$, and ρ represents the subsurface resistivity distribution. The second term on the right side represents the model smoothness constraint term, which suppresses abrupt variations between model parameters. Here, $\lambda_{\rho s}$ denotes the smoothness constraint factor for model parameters, playing a crucial role in inversion resolution and stability, while $\boldsymbol{S}$ represents the smoothness constraint matrix. The third term on the right-hand side constitutes the model background constraint term, which serves to drive the inversion model toward a homogeneous model. Here, $\lambda_{\rho b}$ represents the background or known property constraint factor for model parameters, while $\boldsymbol{B}$ denotes the background or known property constraint matrix (a diagonal matrix).

Differentiating both sides of Equation (3) with respect to the model parameters and setting the derivatives equal to zero yields the following generalized linear inversion equation for resistivity:

$$({\boldsymbol{J}_\rho}^T {\boldsymbol{W}_\rho}^T \boldsymbol{W}_\rho \boldsymbol{J}_\rho + \lambda_{\rho s} \boldsymbol{S}^T \boldsymbol{S} + \lambda_{\rho b} \boldsymbol{B}^T \boldsymbol{B}) \Delta \boldsymbol{m}_\rho = \boldsymbol{J}^T {\boldsymbol{W}_\rho}^T \Delta \boldsymbol{d}_\rho - \lambda_{\rho s} \boldsymbol{S}^T \boldsymbol{S} \boldsymbol{m}_\rho + \lambda_{\rho b} \boldsymbol{B}^T \boldsymbol{B} (\boldsymbol{m}_{\rho b} - \boldsymbol{m}_\rho) \tag{4}$$

where $J_\rho = \left[\partial d_{\rho ci}/\partial m_j\right]$ represents the partial derivative matrix of simulated data with respect to model parameters. The primary computation methods include the reciprocity principle method (computationally intensive and memory-demanding) and the quasi-Newton method (computationally efficient). In practice, these two approaches are often combined, with the choice between them depending on the scale of the inversion problem. $\Delta \boldsymbol{d}_\rho = \boldsymbol{d}_{\rho a} - \boldsymbol{d}_{\rho c}$ denotes the data residual vector. The conjugate gradient method is typically employed to solve Equation (4), yielding the model parameter update $\Delta \boldsymbol{m}_\rho$. Through multiple inversion iterations, the subsurface resistivity model $\boldsymbol{m}_\rho$ can be obtained and substituted into the following equation:

$$m_{\rho 1} = m_{\rho 0} + u * \Delta m_\rho \tag{5}$$

In Equation (5), u represents the correction factor for the iteration step length. The 0.618 golden section search method is employed to determine a suboptimal correction factor u. Subsequently, the model parameters for the next inversion iteration can be computed using Equation (5), followed by model updating. This iterative process continues until the mean squared error converges to meet the predefined criteria, ultimately yielding the subsurface resistivity model m_ρ.

Building upon this foundation, a linear inversion method for chargeability (applicable when chargeability values are relatively small) was employed by solving a single linear inversion equation, and the subsurface chargeability model can be obtained as follows:

$$(\boldsymbol{J}_\rho{}^T \boldsymbol{W}_\eta{}^T \boldsymbol{W}_\eta \boldsymbol{J}_\rho + \lambda_{\eta s} \boldsymbol{S}^T \boldsymbol{S} + \lambda_{\eta b} \boldsymbol{B}^T \boldsymbol{B}) \boldsymbol{\eta} = \boldsymbol{J}_\rho{}^T \boldsymbol{W}_\eta{}^T \boldsymbol{\eta}_a + \lambda_{\eta b} \boldsymbol{B}^T \boldsymbol{B} \boldsymbol{\eta}_b \tag{6}$$

where $\boldsymbol{W}_\eta$ is the chargeability weighting matrix, $\boldsymbol{\eta}$ represents the chargeability model parameters, $\boldsymbol{\eta}_a$ denotes the measured chargeability data, $\boldsymbol{\eta}_b$ stands for the background chargeability distribution, $\lambda_{\eta s}$ and $\lambda_{\eta b}$ are respectively the smoothing and background constraint factors for chargeability inversion, and $\boldsymbol{J}_\rho$ is the partial derivative matrix that has been previously computed during resistivity inversion, resulting in significantly reduced computational cost for the linear chargeability inversion.

When subsurface polarizability parameters are sufficiently large such that the measured apparent polarizability and polarizability model exhibit nonlinear relationships, the objective function for polarizability inversion is similarly constructed under the least squares criterion as follows:

$$\Phi_\eta(\boldsymbol{m}_\eta) = \left\| \boldsymbol{W}_\eta \left[\boldsymbol{d}_{\eta a} - \boldsymbol{d}_{\eta c}(\boldsymbol{m}_\eta) \right] \right\|_2{}^2 + \lambda_{\eta s} \left\| \boldsymbol{S} \boldsymbol{m}_\eta \right\|_2{}^2 + \lambda_{\eta b} \left\| \boldsymbol{B} \left[\boldsymbol{m}_\eta - \boldsymbol{m}_{\eta b} \right] \right\|_2{}^2 \tag{7}$$

The parameters are analogous to those in Equation (3). By differentiating both sides of Equation (7) with respect to the model parameters and setting the derivatives to zero, the generalized linear inversion equation for polarizability can be derived thusly:

$$(\boldsymbol{J}_\eta{}^T \boldsymbol{W}_\eta{}^T \boldsymbol{W}_\eta \boldsymbol{J}_\eta + \lambda_{\eta s} \boldsymbol{S}^T \boldsymbol{S} + \lambda_{\eta b} \boldsymbol{B}^T \boldsymbol{B}) \Delta \boldsymbol{m}_\eta = \boldsymbol{J}^T \boldsymbol{W}_\eta{}^T \Delta \boldsymbol{d}_\eta - \lambda_{\eta s} \boldsymbol{S}^T \boldsymbol{S} \boldsymbol{m}_\eta + \lambda_{\eta b} \boldsymbol{B}^T \boldsymbol{B} (\boldsymbol{m}_{\eta b} - \boldsymbol{m}_\eta) \tag{8}$$

By solving Equation (8), the polarizability model parameter update $\Delta \boldsymbol{m}_\eta$ can be obtained and substituted into the following equation:

$$m_{\eta 1} = m_{\eta 0} + u * \Delta m_\eta \tag{9}$$

The 0.618 golden section search method is implemented to determine a suboptimal correction factor u. This factor is then substituted into Equation (9) to compute the updated model parameters for the subsequent inversion iteration. Following model updating, the it-

erative process continues until the mean squared error satisfies the predefined convergence criteria, ultimately yielding the final subsurface resistivity model m_η.

The workflow of the spread-spectrum induced polarization equivalent inversion algorithm is illustrated in Figure 3.

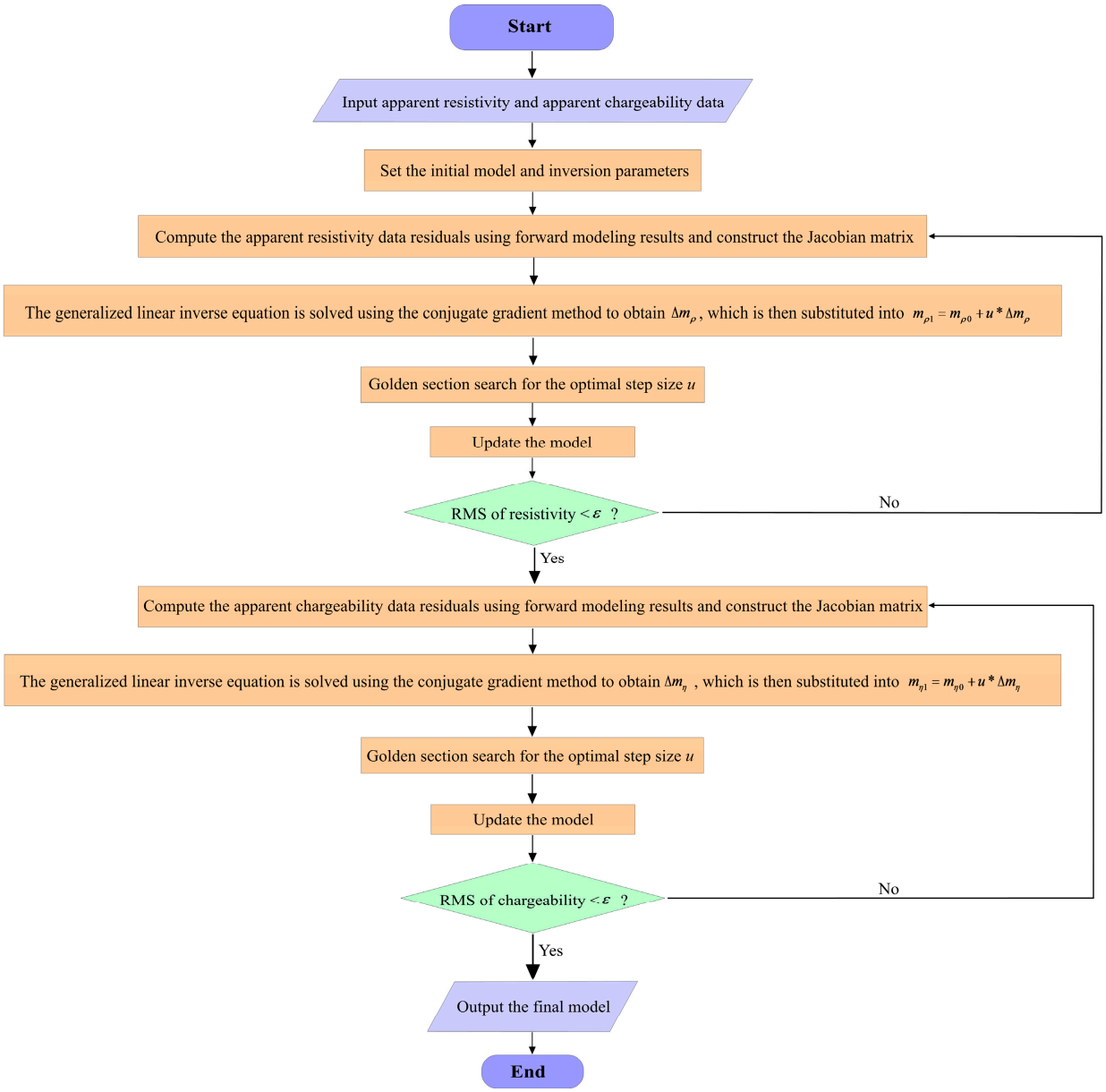

Figure 3. Flowchart of the equivalent inversion algorithm.

The Lagrange multiplier, also known as the damping factor or regularization parameter, plays a pivotal role in inversion. During the inversion process, it is assumed that the Lagrange multiplier (λ) selected for each iteration is reasonably chosen. This ensures an optimal trade-off between solution variance and resolution while guaranteeing that the error convergence curve exhibits steady descent, initially decreasing rapidly in early iterations before slowing down significantly, and the convergence criterion for iterative inversion is that the error convergence curve no longer decreases when the set number of iterations is reached. Consequently, an approximately ideal sequence of λ values can be constructed to mimic the desired error convergence behavior, allowing the inversion process to gradually relax constraints as the number of iterations increases.

The λ sequence is constructed using Equation (10):

$$\lambda(k) = a \cdot k^{-2} + b \tag{10}$$

The parameter k denotes the iteration index, while a and b are coefficients to be determined. Given the maximum number of inversion iterations (n_{max}) and an initial Lagrange multiplier λ_{max} (the smoothing factor, typically selected between 0.1 and 1 based on the noise level in the data), the minimum Lagrange multiplier (λ_{min}, the background factor) can be set as $\lambda_{min} = \lambda_{max}/10$ for simplicity. This allows the determination of a, b, and the intermediate Lagrange multipliers. In this inversion, we selected $\lambda_{max} = 0.5$, $\lambda_{min} = 0.05$, and $n_{max} = 5$, resulting in the following λ sequence: 0.5, 0.1529, 0.089, 0.066, 0.056, 0.05.

3. Results and Discussion

During data processing, the entire 5200 m profile was subjected to inversion analysis. The central 2000 m segment of the inversion results was then extracted, yielding resistivity and chargeability cross-sections extending to depths of 1200 m below the surface.

Figures 4 and 5 present the resistivity/chargeability inversion results for line L1. The inversion reveals transitional zones between stations 520–620 and 920–1000, likely caused by fracture zones. The resistivity inversion shows minimal near-surface variations, with a 50–150 m thick low-resistivity layer interpreted as clay-rich weathering products. A dike-like high-resistivity anomaly occurs between stations 700 and 850, possibly representing intrusive granitic porphyry or quartz porphyry. Two high-chargeability anomalous zones are identified at stations 80–440 and 950–1100, with shifting anomaly centers flanking the high-resistivity dike and corresponding to low-resistivity zones in the resistivity section. Based on spectral IP characteristics of metallic deposits, the IP anomalies at stations 400 and 1000 most likely originate from massive metallic mineralization, exhibiting typical metallic deposit signatures and potentially representing skarn-type or quartz-vein polymetallic deposits.

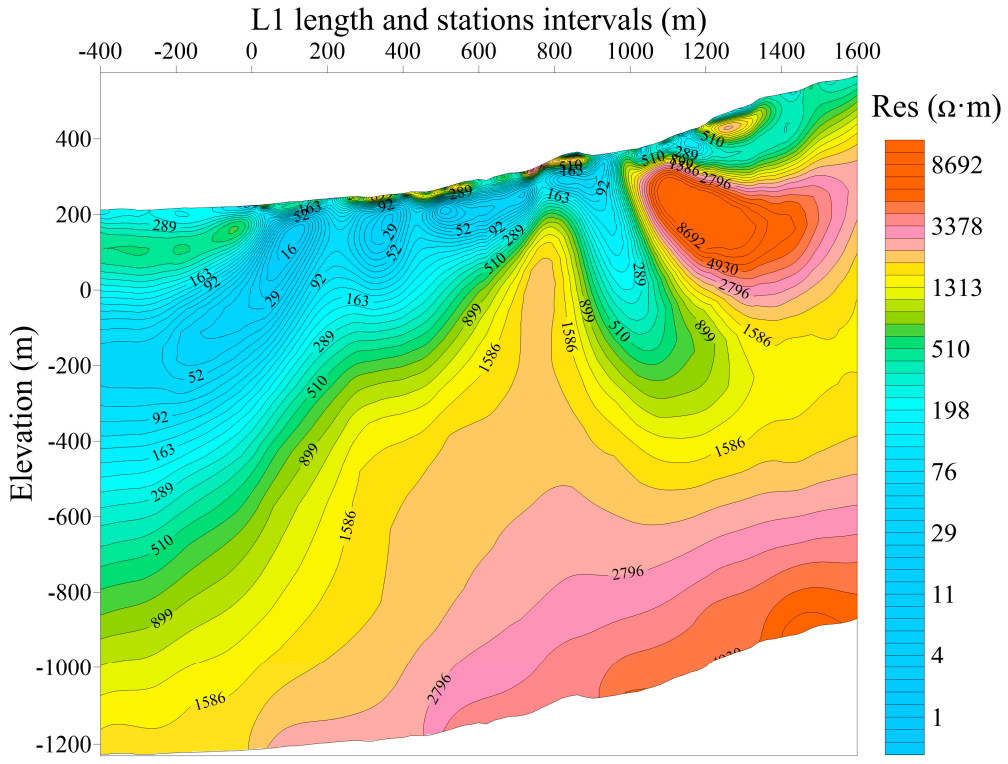

Figure 4. Two-dimensional inversion of the resistivity of the L1 line.

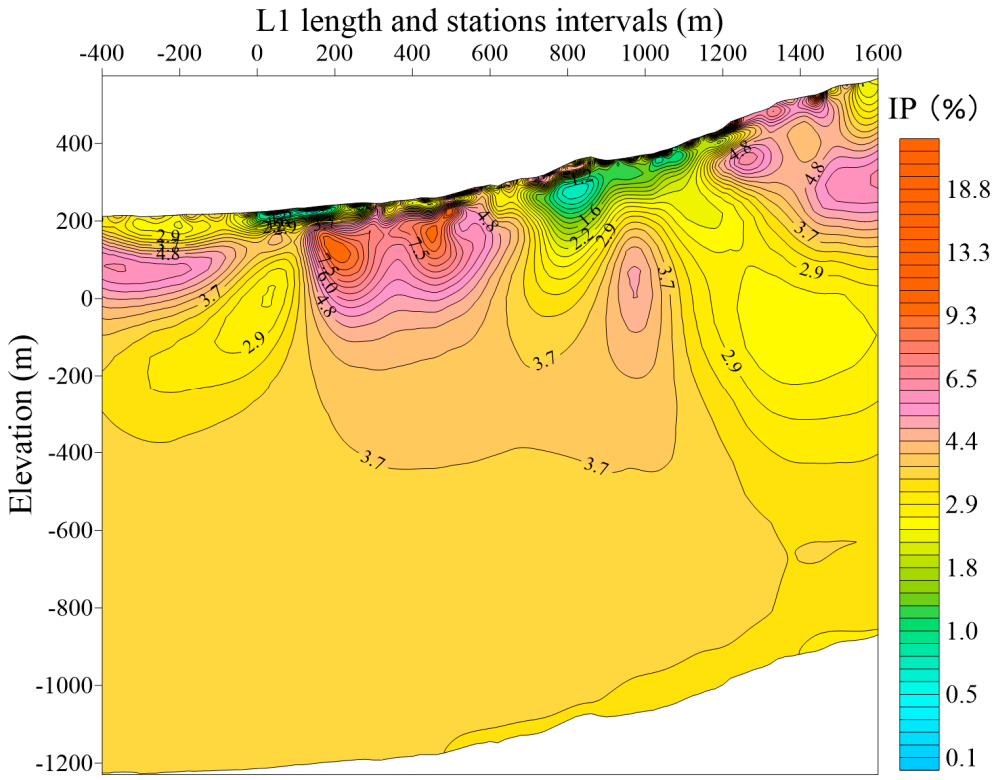

Figure 5. The results of the two-dimensional inversion of the L1 linear width frequency.

The burial depth of the igneous rock top interface gradually becomes shallower from the small mileage to the large mileage direction, with the shallowest granite top interface occurring at about 200 m depth in the section from 1400 m to 1600 m of L1. Based on the resistivity and chargeability anomaly characteristics, the low-resistivity anomaly zones that developed within high-resistivity areas or near high-resistivity anomalies are interpreted as ore veins. So, three ore veins are identified in the L1 geological profile (Figure 6): The skarn-type (Vein A) is located at the contact between volcanic rocks and sedimentary rocks in the section from 200 m to 400 m of L1, showing low-resistivity and high-polarization features with its top interface around 0 m elevation. The greisen-type (Veins A and B) occurs at the contact zone between igneous rocks and sedimentary rocks: Vein B in the section from 500 m to 700 m of L1, exhibiting low-resistivity and high-polarization characteristics with its top interface near 50 m elevation; and Vein C in the section from 850 m to 1100 m of L1, demonstrating low-resistivity and moderate- to low-polarization properties with its top interface at approximately 200 m elevation.

The resistivity/chargeability inversion results for Line L2 are presented in Figures 7 and 8. Between stations 200 and 650, a high-resistivity layer exists beneath the surface, likely caused by shallow quartz sandstone, siltstone, or marble. Below this high-resistivity layer lies a low-resistivity zone, interpreted as Devonian mudstone or shale. A steeply dipping high-resistivity body occurs between stations 740 and 900, possibly representing an intrusive granite dike. The first IP anomaly zone (between stations 700 and 760) exhibits high chargeability and corresponds to a low-resistivity anomaly in the resistivity section, distributed near the intrusive dike and attributed to massive metallic mineralization. The second induced polarization anomaly, located between stations 300 and 500, exhibits a high-resistivity and low-chargeability signature, which is interpreted as limestone in contact with intrusive granite.

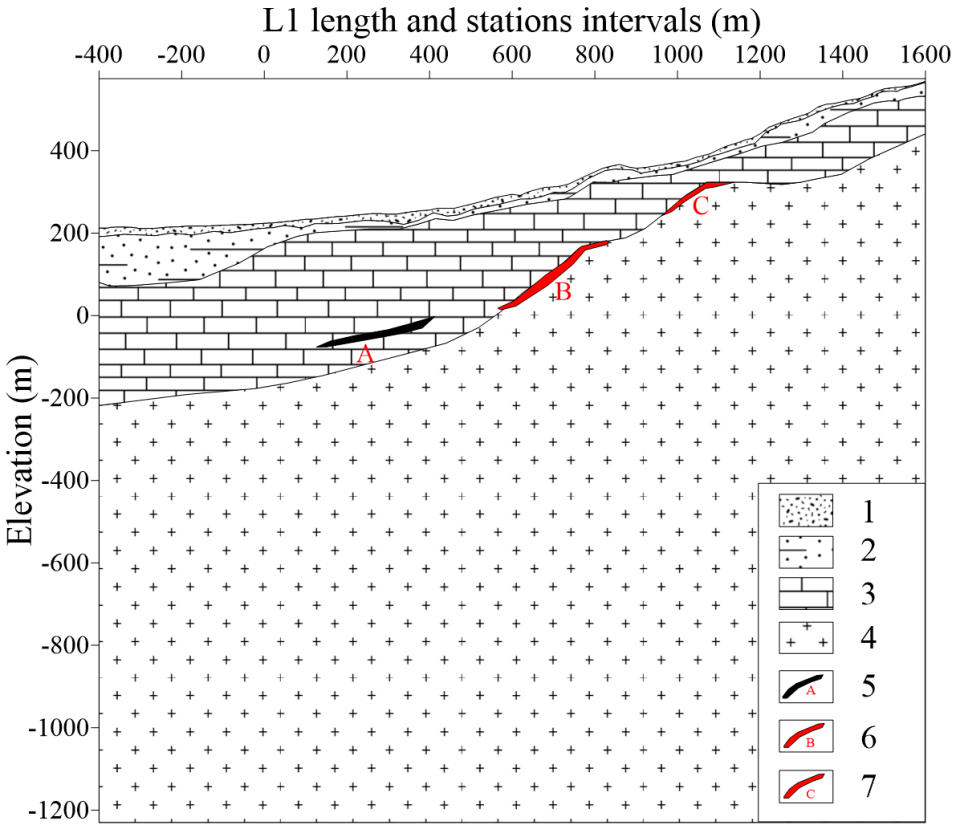

Figure 6. Interpretative geological profile of L1. 1: Weathered layer/quaternary sediments; 2:'sandstone/sandy mudstone; 3: Devonian limestone; 4: medium-fine-grained porphyritic biotite granite; 5: skarn-type W-Sn orebody and its identification letter; 6: greisen-type W-Sn orebody and its identification letter; 7: greisen-type W-Sn orebody and its identification letter.

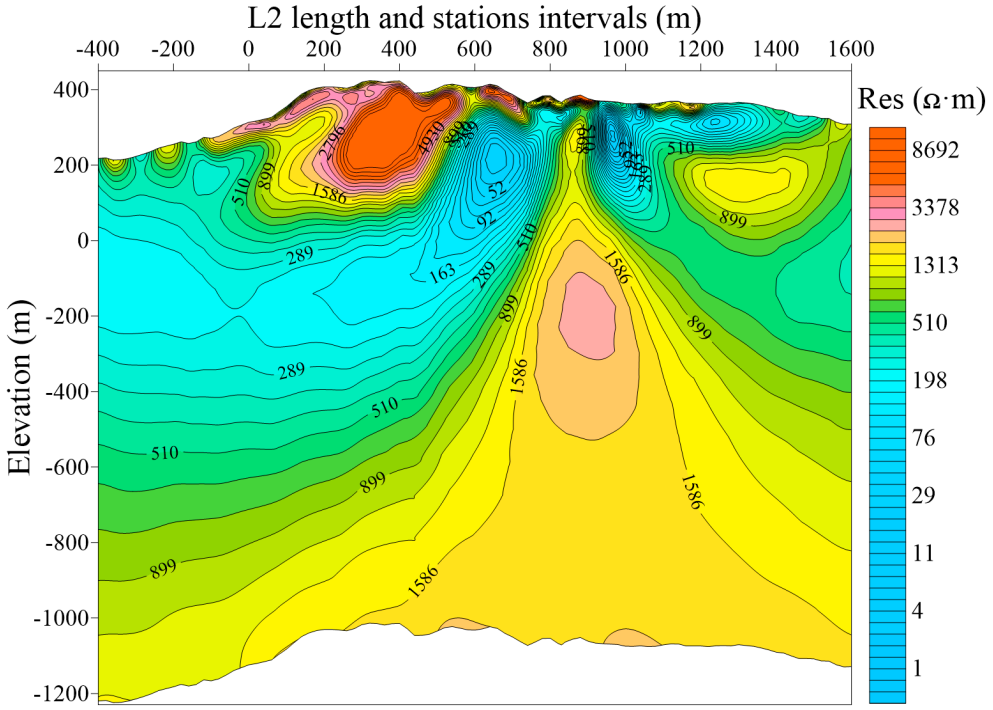

Figure 7. Two-dimensional inversion of the resistivity of the L2 line.

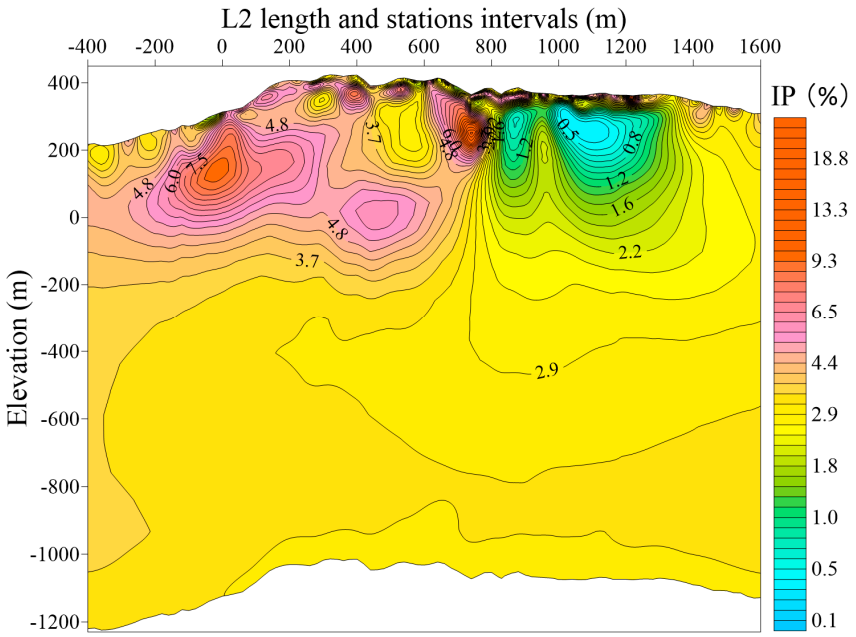

Figure 8. The results of the two-dimensional inversion of the L2 linear width frequency.

The inferred ore veins and rock distribution along Line L2 are shown in Figure 9. Similar to Line L1, the depth of the igneous rock top interface gradually decreases from smaller to larger station numbers, intruding into the country rocks with the top interface at approximately 200 m elevation. Based on resistivity and IP anomaly characteristics, areas exhibiting metallic mineralization IP signatures and low-resistivity anomaly zones within or adjacent to high-resistivity regions are interpreted as ore veins. Three ore veins are identified in this profile: Vein A (skarn-type) is relatively deep (between stations 200 and 400), showing low-resistivity and moderate-chargeability anomalies with its top interface near 0 m elevation; Vein B (greisen-type) develops at the contact between igneous and sedimentary rocks (between stations 600 and 800), exhibiting low-resistivity and high-chargeability anomalies with its top interface near 50 m elevation; Vein C (greisen-type) occurs at the granite–sedimentary rock contact (between stations 970 and 1150), displaying relatively low-resistivity anomalies with its top interface near 100 m elevation.

The intrusion of composite granites and subsequent post-magmatic hydrothermal activities in the study area provided sufficient heat sources for rock and mineral formation. Combined with the relatively abundant W and Sn in the region, these processes supplied ample material sources for mineralization. The contact zones between intrusive granites and country rocks created favorable metallogenic conditions. The delineated greisen-type veins are distributed near the top interface and contact zones of intrusive granites, while the identified skarn-type veins occur in limestone strata contacting granites.

Greisen-type W-Sn deposits are high-temperature pneumatolytic-hydrothermal deposits typically associated with the upper or marginal zones of highly fractionated granites, whereas skarn-type deposits are contact metasomatic deposits predominantly hosted in marble, limestone, and skarn formations. Figure 10 presents the drilling results along the exploration line in the Longshang mining area (Figure 1c), where both skarn-type and quartz vein-type W-Sn veins are developed. The greisen-type W-Sn veins occur in the upper and marginal zones of the granite pluton, while the skarn-type W-Sn veins are hosted within Devonian limestone strata in contact with the granite. The drilling results not only confirm the accuracy of the delineated ore veins but also demonstrate the effectiveness of the large-electrode-spacing multi-channel spread-spectrum induced polarization method in polymetallic mineral exploration.

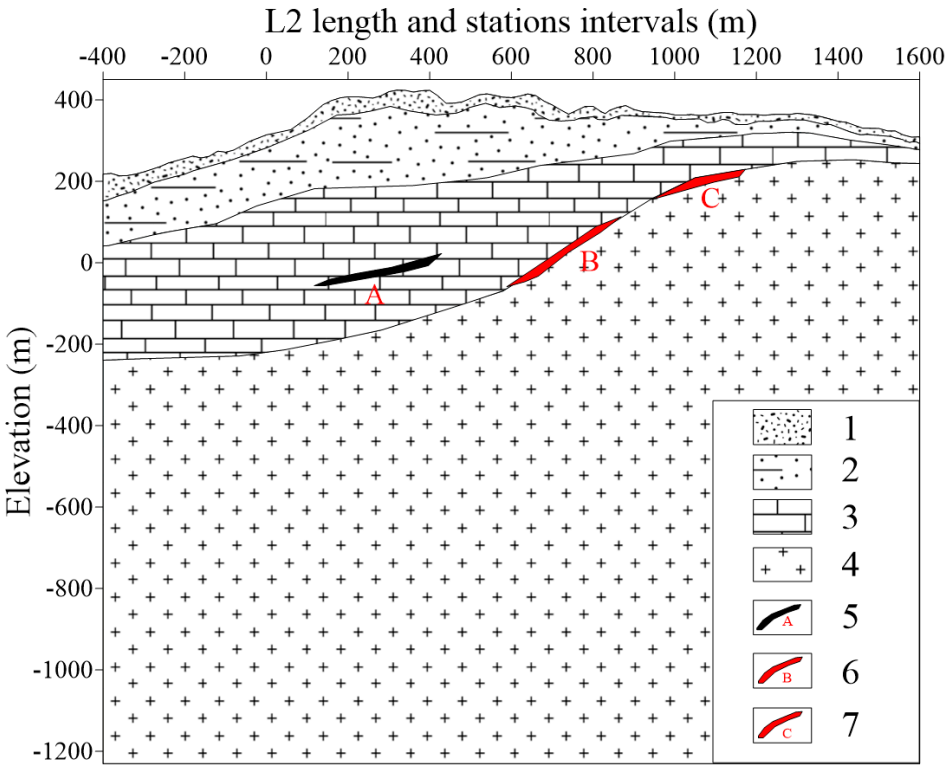

Figure 9. Interpretative geological profile of L2. 1: Weathered layer/quaternary sediments; 2: sandstone/sandy mudstone; 3: Devonian limestone; 4: medium-fine-grained porphyritic biotite granite; 5: skarn-type W-Sn orebody and its identification letter; 6: greisen-type W-Sn orebody and its identification letter; 7: greisen-type W-Sn orebody and its identification letter.

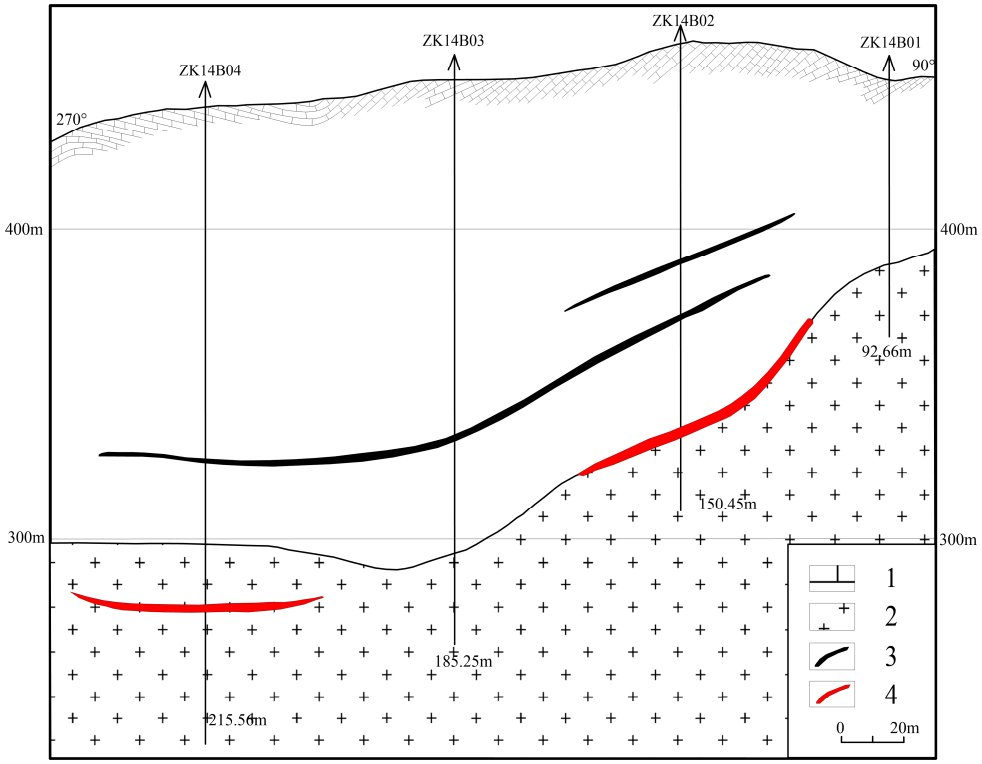

Figure 10. Drilling Results in the Longshang mining district (modified from [14]). 1: Devonian limestone; 2: medium-fine-grained porphyritic biotite granite; 3: skarn-type W-Sn orebody; 4: greisen-type W-Sn orebody.

As an advanced mineral exploration technique, SSIP demonstrates significant advantages over conventional IP, audio-magnetotellurics (AMT), and controlled-source audio-magnetotellurics (CSAMT). Utilizing broadband continuous-signal spectrum analysis, SSIP enables the simultaneous acquisition of multi-frequency data in a single measurement. It offers efficient data collection and full-spectrum dispersion characterization capabilities, making it particularly suitable for mineral exploration in geologically complex regions. However, the method has notable limitations in high-noise environments or areas with strong lateral electrical heterogeneity: noise interference can significantly reduce the signal-to-noise ratio (SNR), while abrupt changes in electrical properties can cause the induced polarization response to deviate from simplified model assumptions, increasing the non-uniqueness in inversion solutions. Additionally, in areas with high grounding noise (e.g., clay-rich layers) or very low-resistivity overburden, SSIP performs poorly. The former greatly reduces the SNR and hampers the identification of dispersion features, while the latter restricts detection depth and induces shielding effects. In such scenarios, supplementary geophysical techniques or data optimization methods are necessary to improve interpretational reliability.

In practical applications, SSIP faces various technical challenges. Electromagnetic coupling effects—including capacitive and inductive coupling—can significantly distort IP signals in low-resistivity regions or under large electrode spacing, leading to phase and amplitude frequency response distortions. For example, coupling effects in high-frequency ranges may completely obscure genuine IP responses. Data processing is also complex: although time–domain exponential function fitting can partially preserve IP information, it is sensitive to outliers such as anomalous time segments and requires optimization using frequency–domain analysis or additional filtering techniques. Frequency selection is particularly critical, as different ore types (e.g., massive versus disseminated ore) exhibit distinct characteristic frequencies. Improper frequency selection may result in weakened anomaly responses or even missed targets. Environmental factors such as increased distributed capacitance in humid areas and industrial stray currents further degrade data quality, necessitating corrective technical measures.

To fully exploit the strengths of SSIP while overcoming its limitations, several key aspects must be addressed during field implementation. First, frequency selection and instrument configuration must be optimized based on the characteristics of the target deposit (low frequencies for massive ores, high frequencies for disseminated ores), and electromagnetic coupling suppression should be considered when determining working frequencies. During fieldwork, grounding resistance must be minimized by employing parallel electrode configurations or using water infiltration techniques to improve the grounding of current electrodes. Laying cables in moist environments should be avoided; where necessary, cables should be elevated above ground to reduce capacitive coupling. For data processing, it is advisable to combine time–domain fitting (e.g., exponential decoupling) with frequency–domain analysis (e.g., multi-frequency phase correction), and to incorporate machine-learning algorithms for automatic identification of anomalous data points, thereby enhancing interpretational accuracy. Moreover, survey results should be validated through drilling or known geological cross-sections and analyzed using multiple parameters (e.g., phase, dispersion rate, and relative phase) to avoid misinterpretation based on single-parameter analysis. In areas with strong industrial interference, measurements should be conducted during off-peak hours, and data averaging across multiple acquisitions should be employed to suppress noise. Regular instrument calibration is also essential to ensure data reliability.

Future developments in SSIP technology should focus on several goals: improving SNR through hardware upgrades, multi-channel synchronous acquisition, and algorithms

for correcting electrical heterogeneities; integrating AMT/CSAMT data for joint inversion to overcome current technical limitations; establishing three-dimensional observation systems and developing joint time–frequency inversion methods to enhance deep-resolution capabilities; deploying high-density electrode arrays in mineralized anomaly zones to better delineate boundary changes in electrical properties; conducting laboratory spectral IP experiments on core samples; and integrating gravity and magnetic data to perform joint multi-physics inversion. These enhancements will not only improve the spatial accuracy of orebody delineation but also allow for indirect estimation of enrichment levels of minerals such as tungsten and tin, providing a more reliable scientific basis for deep resource evaluation. Application examples from the Xitian tin deposit indicate that large-array, multi-channel SSIP technology has successfully detected deep tungsten–tin orebodies; however, it still faces limitations such as restricted resolution, strong inversion non-uniqueness, and insufficient spatial coverage. These findings highlight the need for stronger geological and drilling constraints in subsequent work, increased profile density to improve spatial coverage, and careful consideration of topographic and electromagnetic interference effects on data quality.

4. Conclusions

(1) The SSIP method conducts multi-channel array measurements in both spatial and frequency domains, achieving an observational efficiency three- to five-times higher than conventional symmetrical quadrupole IP sounding. For a single survey line (1200 m), data acquisition time can be reduced to 1/3 of traditional methods, significantly lowering field time costs. Through surveys along two lines, an average exploration depth of 1200 m was attained, representing an approximately 50% improvement over conventional IP methods (typically <800 m).

(2) Drilling verification results demonstrate high consistency in both spatial positioning and burial depth between the three ore veins delineated by SSIP anomalies and the orebodies intercepted by drilling. The predicted orebodies show comparable dimensions and strike lengths to those confirmed by drilling.

(3) The inferred mineralization-related anomalies exhibit low-resistivity/high-chargeability or low-resistivity/moderate-chargeability characteristics in inversion sections. According to vein distribution patterns, greisen-type W-Sn veins (e.g., Veins A and C) tend to be concentrated at the top interface of intrusive granites and their contact zones, while skarn-type W-Sn veins (e.g., Vein B) predominantly occur in limestone and marble strata contacting granites. These findings provide quantitative references for deep prospecting in similar metallogenic geological settings.

Author Contributions: Conceptualization, X.L. and H.L.; methodology, H.L.; software, Y.Z. (Yingjie Zhao); validation, X.L., H.L. and Y.Z. (Yuhao Zhang); formal analysis, Y.Z. (Yingjie Zhao); investigation, X.L. and D.Z.; resources, H.L.; data curation, Y.Z. (Yuhao Zhang); writing—original draft preparation, X.L.; writing—review and editing, H.L. and Y.Z. (Yingjie Zhao); visualization, Y.Z. (Yuhao Zhang); supervision, H.L.; project administration, H.L.; funding acquisition, H.L. All authors have read and agreed to the published version of the manuscript.

Funding: National Natural Science Foundation of China (41774149); Project of Hunan Provincial Department of Ecology and Environment (HBKYXM-2023032); Hunan Provincial Science and Technology Program (2024SKY-003).

Institutional Review Board Statement: Not applicable.

Informed Consent Statement: Not applicable.

Data Availability Statement: The original contributions presented in the study are included in the article, further inquiries can be directed to the corresponding author.

Conflicts of Interest: The authors declare no conflict of interest.

References

1. Mao, J.; Pirajno, F.; Cook, N. Mesozoic metallogeny in East China and corresponding geodynamic settings-An introduction to the special issue. *Ore Geol. Rev.* **2011**, *43*, 1–7. [CrossRef]
2. Soloviev, S.G.; Kryazhev, S.G.; Dvurechenskaya, S.S. Geology, mineralization, and fluid inclusion characteristics of the Lermontovskoe reduced-type tungsten (Cu, Au, Bi) skarn deposit, Sikhote-Alin, Russia. *Ore Geol. Rev.* **2017**, *89*, 15–39. [CrossRef]
3. Mao, J.W.; Xie, G.Q.; Guo, C.L.; Yuan, S.D.; Cheng, Y.B.; Chen, Y.C. Spatial-temporal distribution of Mesozoic ore deposits in south China and their metallogenic settings. *Geol. J. China Univ.* **2008**, *14*, 510–526.
4. Neiva, A.M.R. Geochemistry of cassiterite and wolframite from tin and tungsten quartz veins in Portugal. *Ore Geol. Rev.* **2008**, *33*, 221–238. [CrossRef]
5. Mao, J.W.; Xie, G.Q.; Guo, C.L.; Chen, Y.C. Large-scale tungsten-tin mineralization in the Nanling region, South China: Metallogenic ages and corresponding geodynamic processes. *Acta Petrol. Sin.* **2007**, *23*, 2329–2338.
6. Moura, A.; Dória, A.; Neiva, A.M.R.; Leal Gomes, C.; Creaser, R.A. Metallogenesis at the Carris W-Mo-Sn deposit (Gerês, Portugal): Constraints from fluid inclusions, mineral geochemistry, Re-Os and He-Ar isotopes. *Ore Geol. Rev.* **2014**, *56*, 73–93. [CrossRef]
7. Cheng, Y.; Mao, J.; Liu, P. Geodynamic setting of Late Cretaceous Sn-W mineralization in southeastern Yunnan and northeastern Vietnam. *Solid Earth Sci.* **2016**, *1*, 79–88. [CrossRef]
8. Chicharro, E.; Boiron, M.; López-García, J.Á.; Barfod, D.N.; Villaseca, C. Origin, ore forming fluid evolution and timing of the Logrosán Sn-(W) ore deposits (Central Iberian Zone, Spain). *Ore Geol. Rev.* **2016**, *72*, 896–913. [CrossRef]
9. Kempe, U.; Wolf, D. Anomalously high Sc contents in ore minerals from Sn-W deposits: Possible economic significance and genetic implications. *Ore Geol. Rev.* **2006**, *28*, 103–122. [CrossRef]
10. Liu, P.; Mao, J.; Cheng, Y.; Yao, W.; Wang, X.; Hao, D. An Early Cretaceous W-Sn deposit and its implications in southeast coastal metallogenic belt: Constraints from U-Pb, Re-Os, Ar-Ar geochronology at the Feie'shan W-Sn deposit, SE China. *Ore Geol. Rev.* **2017**, *81*, 112–122. [CrossRef]
11. Soloviev, S.G.; Kryazhev, S.G.; Dvurechenskaya, S.S. Geology, mineralization, stable isotope, and fluid inclusion characteristics of the Vostok-2 reduced W-Cu skarn and Au-W-Bi-As stockwork deposit, Sikhote-Alin, Russia. *Ore Geol. Rev.* **2017**, *86*, 338–365. [CrossRef]
12. Zhang, Y.; Yang, J.; Chen, J.; Wang, H.; Xiang, Y. Petrogenesis of Jurassic tungsten-bearing granites in the Nanling Range, South China: Evidence from whole-rock geochemistry and zircon U-Pb and Hf-O isotopes. *Lithos* **2017**, *278*, 166–180. [CrossRef]
13. Zhao, W.W.; Zhou, M.; Li, Y.H.M.; Zhao, Z.; Gao, J. Genetic types, mineralization styles, and geodynamic settings of Mesozoic tungsten deposits in South China. *J. Asian Earth Sci.* **2017**, *137*, 109–140. [CrossRef]
14. Liang, X.; Dong, C.; Jiang, Y.; Wu, S.; Zhou, Y.; Zhu, H.; Fu, J.; Wang, C.; Wang, C. Zircon U-Pb, molybdenite Re-Os and muscovite Ar-Ar isotopic dating of the Xitian W-Sn polymetallic deposit, eastern Hunan Province, South China and its geological significance. *Ore Geol. Rev.* **2016**, *78*, 85–100. [CrossRef]
15. Hsu, K.-C. Tungsten deposits of southern Kiangsi, China. *Econ. Geol.* **1943**, *38*, 431–474. [CrossRef]
16. Lu, H.Z. *The Origin of Tungsten Mineral Deposits in South China*; Chongqing Publishing House: Chongqing, China, 1986.
17. Jingwen, M.; Yanbo, C.; Maohong, C.; Pirajno, F. Major types and time–space distribution of Mesozoic ore deposits in South China and their geodynamic settings. *Min. Depos.* **2013**, *48*, 267–294. [CrossRef]
18. Mao, Z.; Cheng, Y.; Liu, J.; Yuan, S.; Wu, S.; Xiang, X.; Luo, X. Geology and molybdenite Re-Os age of the Dahutang granite-related veinlets-disseminated tungsten ore field in the Jiangxin Province, China. *Ore Geol. Rev.* **2013**, *53*, 422–433. [CrossRef]
19. Wu, S.C.; Long, Z.Q.; Zeng, G.H.; Long, W.P. Prospecting progress and potential of Sn-Pb-Zn polymetallic deposits in Xitian area, Hunan Province. *Geol. Miner. Resour. South China* **2011**, *27*, 100–104.
20. Wu, S.C.; Luo, H.W.; Huang, T. Metallogenetic geological characteristics and prospecting of tin-polymetallic deposits in central Xitian area, eastern Hunan. *Geol. Miner. Resour. South China* **2004**, *2*, 21–26.
21. Fu, J.M.; Wu, S.C.; Xu, D.M. Reconstraint from zircon SHRIMP U-Pb dating on the age of magma intrusion and mineralization in Xitian tungsten-tin polymetallic orefield, eastern Hunan Province. *Geol. Miner. Resour. South China* **2009**, *3*, 1–7.
22. Fu, J.M.; Cheng, S.B.; Lu, Y.Y. Geochronology of the greisen-quartz-vein type tungsten-tin deposit and its host granite in Xitian, Hunan Province. *Geol. Explor.* **2012**, *48*, 313–320.
23. Abraham, E.M.; Uwaezuoke, A.E.; Usman, A.O. Geophysical investigation of subsurface mineral potentials in North-Central Nigeria: Implications for sustainable mining and development. *Geomech. Geophys. Geo-Energy Geo-Resour.* **2024**, *10*, 1–25. [CrossRef]

24. Sultan, S.A.; Mansour, S.A.; Santos, F.M.; Helaly, A.S. Geophysical exploration for gold and associated minerals, case study: Wadi El Beida area, South Eastern Desert, Egypt. *J. Geophys. Eng.* **2009**, *6*, 345–356. [CrossRef]
25. Wynn, J.C. Titanium geophysics: The application of induced polarization to sea-floor mineral exploration. *Geophysics* **1988**, *53*, 386–401. [CrossRef]
26. Di, Q.; Xue, G.; Lei, D.; Zeng, Q.; Fu, C.; An, Z. Summary of technology for a comprehensive geophysical exploration of gold mine in North China Craton. *Sci. China Earth Sci.* **2021**, *64*, 1524–1536. [CrossRef]
27. Walter, C.; Braun, A.; Fotopoulos, G. High-resolution unmanned aerial vehicle aeromagnetic surveys for mineral exploration targets. *Geophys. Prospect.* **2020**, *68*, 334–349. [CrossRef]
28. Yin, Y.; Chen, J.; Zhao, Z.; Yang, Y.; Li, C.; Li, H.; Zhao, X. Integrated geophysical prospecting for deep ore detection in the Yongxin gold mining area, Heilongjiang, China. *Sci. Rep.* **2025**, *15*, 7258. [CrossRef]
29. Ye, Z.; Gao, L.; Li, Y.; Chen, C.; Xia, F.; Li, S.; Zhu, Y. Prospecting model and deep mineralization predictions for the Lamasu-Saibo copper deposit based on combined geological and geophysical exploration information. *Ore Geol. Rev.* **2025**, *176*, 106443. [CrossRef]
30. Melo, A.T.; Sun, J.; Li, Y. Geophysical inversions applied to 3D geology characterization of an iron oxide copper-gold deposit in Brazil. *Geophysics* **2017**, *82*, K1–K13. [CrossRef]
31. Arinze, I.J.; Emedo, C.O. Integrated geophysical investigation for shallow-scale massive (Pb-Zn) sulphide and barite exploration in the Abakaliki and Obubra Mining Districts (AOMD), Southeastern Nigeria. *Min. Metall. Explor.* **2021**, *38*, 381–395. [CrossRef]
32. Chen, W.; Liu, H.; Liu, J.; Sun, X.; Zeng, Q. Integrated geophysical exploration for the Longtoushan Ag-Pb-Zn deposit in the southeast of the Da Xing'an Ling mountains, Inner Mongolia, northern China. *Explor. Geophys.* **2010**, *41*, 279–288. [CrossRef]
33. Bauman, P. 2-D resistivity surveying for hydrocarbons-A primer. *Cseg Rec.* **2005**, *30*, 25–33.
34. Legault, J.M.; Carriere, D.; Petrie, L. Synthetic model testing and distributed acquisition dc resistivity results over an unconformity uranium target from the Athabasca Basin, northern Saskatchewan. *Lead. Edge* **2008**, *27*, 46–51. [CrossRef]
35. White, R.M.S.; Collins, S.; Denne, R.; Hee, R.; Brown, P. A new survey design for 3D IP inversion modelling at Copper Hill. *Explor. Geophys.* **2001**, *32*, 152–155. [CrossRef]
36. Jia, L.; Zhang, Q. Application of joint inversion of Wenner and pole-dipole arrays in limestone exploration. *Carbonates Evaporites* **2023**, *38*, 61. [CrossRef]
37. Alfouzan, F.A.; Alotaibi, A.M.; Cox, L.H.; Zhdanov, M.S. Spectral induced polarization survey with distributed array system for mineral exploration: Case study in Saudi Arabia. *Minerals* **2020**, *10*, 769. [CrossRef]
38. Yang, Y.; Zhang, G.; Yao, C.; Deng, Z.; Ren, Z.; Li, C. Application of induced polarization method in mineral resource exploration. *Sustainability* **2023**, *15*, 3840. [CrossRef]
39. Ullah, F.; Zhou, X.; Chen, R.; Yang, L.; Yao, H.; Hu, H.; Chen, S.; Wang, Q. Cu-Polymetallic Deposit Exploration under Thick Cover in Gucheng-Yaxi Area Using Audio-Magnetotelluric and Spread-Spectrum-Induced Polarization. *Minerals* **2024**, *14*, 846. [CrossRef]
40. Zaid, H.A.H.; Arifin, M.H.; Kayode, J.S.; Basori, M.B.I.; Umor, M.R.; Hazim, S.H. Application of 2-D electrical resistivity imaging, and induced polarization methods for delineating gold mineralization at Felda Chiku 3, Kelantan, Malaysia. *Sains Malays.* **2023**, *52*, 305–320. [CrossRef]
41. Casulla, M.A.A.; Mizunaga, H. Characterization of potential Cu-Au mineralization using electrical resistivity and induced polarization methods: A case study in Eastern Labo, Bicol, Philippines. *J. Geophys. Eng.* **2023**, *20*, 411–425. [CrossRef]
42. Irawan, S.D.; Sumintadireja, P.; Saepuloh, A. 2-D subsurface ImagingTechniques for deep ore mineral mapping using geoelectrical and induced polarization (IP) methods. *Procedia Earth Planet. Sci.* **2013**, *6*, 139–144. [CrossRef]
43. Wu, C.; Zou, C.; Peng, C.; Liu, Y.; Wu, T.; Zhou, J.; Tao, C. Numerical simulation study on the relationships between mineralized structures and induced polarization properties of seafloor polymetallic sulfide rocks. *Minerals* **2022**, *12*, 1172. [CrossRef]
44. Adrian, J.; Tezkan, B.; Candansayar, M.E. Exploration of a copper ore deposit in Elbistan/Turkey using 2D inversion of the time-domain induced polarization data by using unstructured mesh. *Pure Appl. Geophys.* **2022**, *179*, 2255–2272. [CrossRef]
45. Embeng, S.B.N.; Meying, A.; Ndougsa-Mbarga, T.; Moreira, C.A.; Amougou, O.U.O. Delineation and quasi-3D modeling of gold mineralization using self-potential (SP), electrical resistivity tomography (ERT), and induced polarization (IP) methods in Yassa Village, Adamawa, Cameroon: A case study. *Pure Appl. Geophys.* **2022**, *179*, 795–815. [CrossRef]
46. Augie, A.I.; Salako, K.A.; Rafiu, A.A.; Jimoh, M.O. Integrated Geophysical Investigation for Potential Gold Mineralised Zone within Lower Part of Zuru Schist Belts, NW Nigeria. *Niger. J. Phys.* **2024**, *33*, 1–14. [CrossRef]
47. Liao, F.; Liu, G.; Zhou, J.; Huang, J.; Xu, J.; Chen, R. Analysis of exploration effect of spread spectrum induced polarization (SSIP) method—Taking the exploration of Dongxiangqiao manganese deposit in Lingling district, Yongzhou City, Hunan Province as an example. *Miner. Explor.* **2024**, *15*, 1691–1699.
48. Zhang, B.; Guo, Z.; Liu, J.; Liu, C.; Yang, M.; Wang, Y. Application of multiscale electromagnetic joint methods in deep karst detection in phosphorus pines in Guizhou Province. *Miner. Explor.* **2024**, *9*, 1653–1660.

49. Cao, J.; Wu, Q.; Yang, X.; Kong, H.; Li, H.; Xi, X.; Huang, Q.; Liu, B. Geochronology and genesis of the Xitian W-Sn polymetallic deposit in eastern Hunan Province, South China: Evidence from zircon U-Pb and muscovite Ar-Ar dating, petrochemistry, and wolframite Sr-Nd-Pb isotopes. *Minerals* **2018**, *8*, 111. [CrossRef]
50. Bai, X.J.; Liu, M.; Hu, R.G.; Fang, Y.; Liu, X.; Tang, B.; Qiu, H.N. Well-Constrained mineralization ages by integrated 40Ar/39Ar and U-Pb dating techniques for the Xitian W-Sn polymetallic deposit, South China. *Econ. Geol.* **2022**, *117*, 833–852. [CrossRef]
51. Liu, W.; Chen, R.; Cai, H.; Luo, W.; Revil, A. Correlation analysis for spread-spectrum induced-polarization signal processing in electromagnetically noisy environments. *Geophysics* **2017**, *82*, E243–E256. [CrossRef]
52. Ahmad, J.; Chen, R.; Ahmed, I.; Yaseen, M.; Shah, S.A.; Rahim, O.A.; Ullah, F.; Fahad, S.; Rui, L. Spread Spectrum Induced Polarization (SSIP) Survey for the Qiushuwan Copper-Molybdenum Deposits in Southern Henan Province, China. *Minerals* **2024**, *14*, 934. [CrossRef]

Disclaimer/Publisher's Note: The statements, opinions and data contained in all publications are solely those of the individual author(s) and contributor(s) and not of MDPI and/or the editor(s). MDPI and/or the editor(s) disclaim responsibility for any injury to people or property resulting from any ideas, methods, instructions or products referred to in the content.